Underwater Acoustic Stealth by a Broadband 2-Bit Coding Metasurface

Gaokun Yu,[1,*] Yanping Qiu,[1] Yong Li,[2] Xinlong Wang,[3] and Ning Wang[1]

[1]*College of Information Science and Engineering, Ocean University of China, Qingdao 266100, China*

[2]*Institute of Acoustics, School of Physics Science and Engineering, Tongji University, Shanghai 200092, China*

[3]*Key Laboratory of Modern Acoustics and Institute of Acoustics, Nanjing University, Nanjing 210093, China*

Underwater acoustic stealth is of significance for hiding targets. Since perfect cloaking achieved by carpet cloaks or metasurface carpet cloaks may only be suitable for static targets, here we propose a broadband 2-bit coding metasurface to reduce the scattering cross section (SCS) of an object by the destructive interferences among waves scattered by different coding elements. A simple and easy fabricated design is developed by drilling square holes into a steel plate. Utilizing the antiresonance induced by couplings among four square holes of the unit cell, we achieve an approximate 95.62% fractional bandwidth of acoustic stealth with the SCS reduction below -10 dB, which has been confirmed by both the theoretical prediction and experimental measurement. Compared with the previously proposed underwater acoustic carpet cloaks by the transformation acoustics, the bandwidth of SCS reduction is greatly expanded by the destructive interferences. In addition, simulations have demonstrated that the proposed metasurface may also be suitable for an object with a nonplanar surface.

I. INTRODUCTION

Owing to the development of metamaterials and metasurfaces, the design of cloaking devices has attracted much attention from scientists and engineers. The transformation optics [1,2] provides a way to guide electromagnetic waves around objects, making them undetectable, and this transformation technique [3–8] has also been investigated in the acoustic domain. Although extreme parameters of cloaks appear in the coordinate transformation, an underwater ultrasound experiment of acoustic cloak based on a network of anisotropic acoustic transmission line was carried out [9]. For the practical realization by metamaterials, the linear transformation was adopted to get rid of the stringent requirements of material parameters, and an object placed on the reflective surface can be hidden by an acoustic carpet cloak, which was verified by experiments in air and underwater [10–13]. Owing to the size of carpet cloaks usually comparable with that of hidden objects, metasurface carpet cloaks, which modulate the reflected wavefronts with the cloak shells being thin with respect to the wavelength, have been proposed and verified by experiments [14–20]. In addition, unlike the transformation method, scattering cancellation [21–25] has also been proposed to eliminate the scattering from the hidden object, where the cloak shell can be designed using isotropic materials and the sound energy is allowed to penetrate the object. Although the above two strategies, transformation technique and scattering cancellation can provide a perfect cloaking effect, there still exist some limitations, for example, a reflective surface is needed for carpet cloaks.

Recently, ultrathin acoustic diffusers [26–30] were proposed to create the optimal and predictable sound diffuse reflection in air. Since the incident acoustic energy can be scattered into all directions, acoustic diffusers provide another scheme to hide objects, reducing scattering cross section (SCS) to make a target invisible. However, the extension of acoustic diffuser from air to underwater is not an easy task due to the large acoustic impedance of water. On the other hand, for the metadiffuser based on the quadratic residue sequence [26,27], a large variety of meta-atoms are needed to fabricate an acoustic metadiffuser when the area of the stealth region is large. Fortunately, the rapid development of coding metasurface [31,32] provides a great potential to engineer an underwater acoustic diffuser of large size with a limited variety of meta-atoms. Coding metasurface has demonstrated the flexibility control of electromagnetic waves, and one of its potential application is to reduce the radar cross section of an object [33–38], which is very useful in the military field. Although the concept of coding metasuface was extended to the acoustic domain to manipulate reflected and transmitted wavefronts in air [39–44], its application to underwater acoustic stealth has not been reported.

*gkyu@ouc.edu.cn

The objective of this work is to simplify the previously proposed underwater acoustic cloaking design and broaden the working bandwidth. Different from the concept of the transformation acoustics, we propose a broadband 2-bit coding metasurface to realize underwater acoustic stealth based on the destructive interferences, where the fractional bandwidth (FBW) of SCS reduction below -10 dB is approximate to 95.62%. Owing to the steel material adopted to build unit cells of metasurface, a simple and easy fabricated design is proposed by drilling square holes into a steel plate, and the antiresonance induced by couplings among four square holes of the unit cell is adopted to broaden the working bandwidth of acoustic stealth. Our recent work [45] has demonstrated that the antiresonance can adjust the phase difference between different unit cells to have a linear dependence on frequency, resulting in achromatic focusing, however, the antiresonance here plays a role in controlling the phase difference between different coding metasurface elements ("00," "01," "10," and "11") to have a weak dependence on frequency, leading to a broadband 2-bit coding metasurface. For a large area of stealth region, SCS reduction by the 2-bit coding metasurface in the three-dimensional (3D) space is calculated by our written program code of the boundary integral method, which has been confirmed by the finite-element method for the two-dimensional (2D)

acoustic scattering problem in Ref. [46]. The predicted monostatic SCS reduction is also verified by an underwater experiment.

II. BROADBAND PHASE RESPONSE BY ANTIRESONANCE

We first introduce 2-bit coding metasurface elements, "00," "01," "10," "11" in Fig. 1(a). Ideally, four types of elements in the 2-bit coding metasurface should have phase responses of 0, $\pi/2$, π and $3\pi/2$, corresponding to the "00," "01," "10," and "11" elements, respectively. Note that the absolute phase response of the "00" element may not be zero at a specific frequency, but this case does not affect any physics because the phase can be normalized to zero. Therefore, phase differences between different elements should satisfy the relations, $\phi_{01} - \phi_{00} = \pi/2$, $\phi_{10} - \phi_{00} = \pi$, and $\phi_{11} - \phi_{00} = 3\pi/2$, at the working bandwidth of acoustic stealth, where ϕ_{00}, ϕ_{01}, ϕ_{10}, and ϕ_{11} represent the reflection phases of each element. The reflection phase of each element is controlled by drilling four square holes into a steel plate, and only two depths h_1 and h_2 of holes are chosen for simplification [marked in Fig. 1(a)]. By a particle swarm optimization algorithm [47], it is found that four holes of the same depth denoted as h_{00} can be chosen for the element "00," four holes of the same depth h_{01} for the element "01," and four holes of the
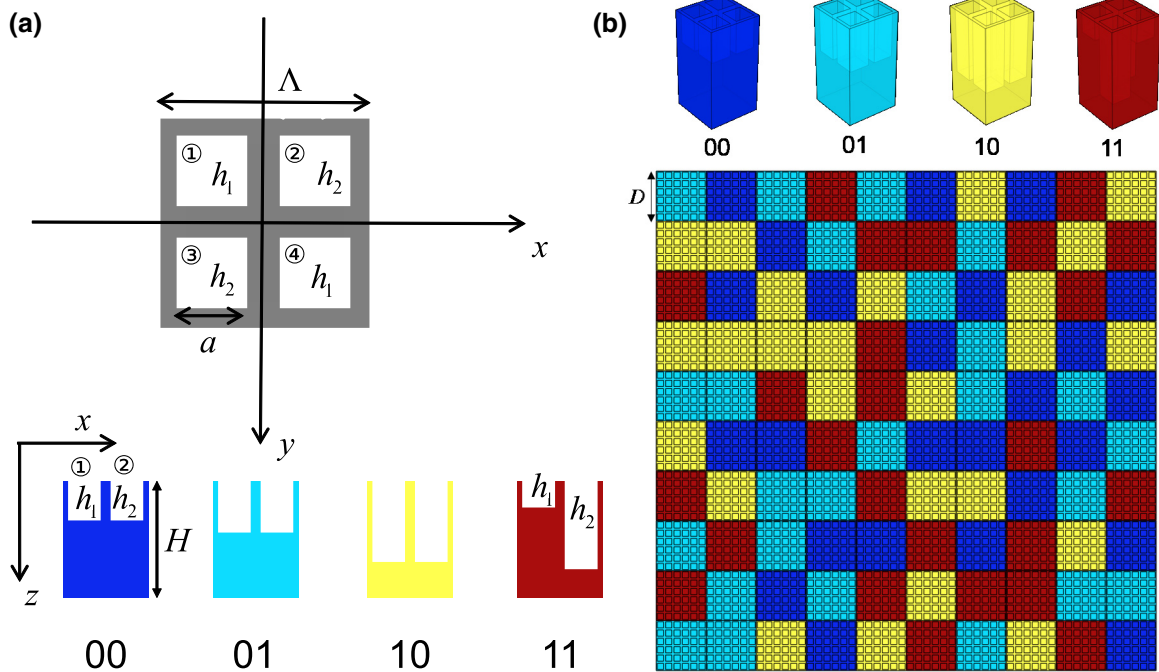

FIG. 1. (a) Schematic diagram of the 2-bit coding metasurface elements, "00," "01," "10," and "11." Each element consists of four square holes drilled into a steel plate of thickness H, where four holes have the same width $a = 0.375\Lambda$, with Λ being the size of the unit cell, and two holes along the diagonal (counterdiagonal) of the unit cell have the same depth h_1 (h_2). (b) Schematic diagram of 2-bit coding metasurface, where each lattice is occupied by a subarray of "00," or "01," or "10," or "11" elements, and the dimension of lattice is $D = 3\Lambda$.

same depth h_{10} for the element "10," where depths satisfy a condition $h_{00} < h_{01} < h_{10}$, while for the element "11," the preferred choice of hole depths is $h_1 \neq h_2$, resulting in the antiresonance.

We assume a normal incident sound wave with the wave number $k = \omega/c_0$, where c_0 represents sound speed in water. Using the temporally harmonic factor $\exp(-j\omega t)$, the reflection phase is obtained by a derivation in Appendix A. Figure 2(a) shows theoretical results of reflection phases of 2-bit coding metasurface elements with the optimized depths of holes. For comparison, the reflection phase of the element "11" is also simulated by the COMSOL Multiphysics software when the elasticity of steel is considered, and there exists a slight difference at the low frequency due to the vibration of steel in water. In order to clearly demonstrate the feature of 2-bit coding, the reflection phase of each element is replotted in the form of phase difference in Fig. 2(b). For the element "11," owing to the coupling among holes of different depths, the antiresonance [marked in Fig. 2(c)] occurs between two resonant frequencies, which are related to the depths h_1 and h_2, respectively. And the antiresonance leads to the curve of reflection phase ϕ_{11} higher than the curves of reflection phases of the other two different types of unit cells, the depth h_2 of which is the same as the element "11." It is also illustrated in Fig. 2(d)

that the existence of antiresonance leads to a broad working bandwidth of element "11" as compared with the unit cells, in which four holes have the same depth. In addition, the distribution of normal velocity v_z for a normal incident wave at the frequency of antiresonance is shown in Fig. 3, where normal velocities along the diagonal and counterdiagonal of the element "11" are out of phase, and the average velocity over the unit cell is zero.

III. THE DESIGN OF 2-BIT CODING METASURFACE AND EXPERIMENTAL CONFIRMATION

Usually, a 2-bit coding metasurface of a given function is realized through a proper arrangement of four types of elements, and its far-field scattering amplitude can be derived by the boundary integral method (see Appendix B) or expressed by the array theory as [32]

$$f(\theta, \varphi; \theta_i, \varphi_i) = f_e(\theta, \varphi; \theta_i, \varphi_i) S(\theta, \varphi; \theta_i, \varphi_i), \quad (1)$$

where $f_e(\theta, \varphi; \theta_i, \varphi_i)$ is the pattern function of an element, (θ, φ) and (θ_i, φ_i) represent the angles of scattered waves and incident waves, respectively, and $S(\theta, \varphi; \theta_i, \varphi_i)$ is the array pattern. Suppose the metasurface consists of an array of $N_x \times N_y$ elements with the size Λ, we obtain

$$S(\theta, \varphi; \theta_i, \varphi_i) = \sum_{n=1}^{N_x} \sum_{m=1}^{N_y} \exp\left[j\Phi(n, m) - jk(\sin\theta\cos\varphi - \sin\theta_i\cos\varphi_i)\left(-\frac{N_x}{2} + n - \frac{1}{2}\right)\Lambda \right.$$
$$\left. -jk(\sin\theta\sin\varphi - \sin\theta_i\sin\varphi_i)\left(-\frac{N_y}{2} + m - \frac{1}{2}\right)\Lambda \right], \quad (2)$$

where $\Phi(n, m)$ represents one of the reflection phases ϕ_{00} ϕ_{01}, ϕ_{10}, and ϕ_{11} at an incident angle (θ_i, φ_i). By a random arrangement of four types of elements, a diffusionlike scattering can be achieved. In order to get an optimized distribution of elements, the directivity $\text{Dir}(\theta, \varphi; \theta_i, \varphi_i)$ is first introduced as,

$$\text{Dir}(\theta, \varphi; \theta_i, \varphi_i) = 4\pi |f(\theta, \varphi; \theta_i, \varphi_i)|^2 \bigg/ \int_0^{2\pi} \int_{\frac{\pi}{2}}^{\pi}$$
$$|f(\theta, \varphi; \theta_i, \varphi_i)|^2 \sin\theta \, d\theta \, d\varphi, \quad (3)$$

where the elevation angle θ of scattered wave ranges from $\pi/2$ to π due to the coordinate system we choose in Fig. 1. We then define SCS reduction (see Appendix C) as

$$\sigma_R = 10\log_{10}\left(\frac{\underset{\theta, \varphi}{\text{Max}}[\text{Dir}(\theta, \varphi; \theta_i, \varphi_i)|_{\text{coded}}]}{\underset{\theta, \varphi}{\text{Max}}[\text{Dir}(\theta, \varphi; \theta_i, \varphi_i)|_{\text{bare}}]} \right), \quad (4)$$

where $\text{Dir}(\theta, \varphi; \theta_i, \varphi_i)|_{\text{coded}}$ represents the directivity of 2-bit coding metasurface and $\text{Dir}(\theta, \varphi; \theta_i, \varphi_i)|_{\text{bare}}$ represents the same sized steel plate. In the following, SCS reduction in Eq. (4) is calculated by two different methods, where one method is based on the boundary integral method, obtaining the far-field scattering amplitude $f(\theta, \varphi; \theta_i, \varphi_i)$ from the scattered field in Appendix B, and the other method is based on the array theory, i.e., using the the array pattern in Eq. (2) and neglecting the effect of pattern function $f_e(\theta, \varphi; \theta_i, \varphi_i)$.

To reduce the computation burden, an optimized distribution of elements [see Fig. 1(b)] is obtained by using a genetic algorithm with a constraint $\sum_{n=1}^{N_x} \sum_{m=1}^{N_y} \exp[j\Phi(n, m)] = 0$ to help SCS reduction, where $N_x = N_y = 30$, the ideal reflection phases 0, $\pi/2$, π and $3\pi/2$ are used for the "00," "01," "10," and "11" elements, respectively, and the array theory is adopted to calculate SCS reduction in the frequency range from $0.2c_0/\Lambda$ to $0.5c_0/\Lambda$. Note that in order to maintain the characteristic of reflection
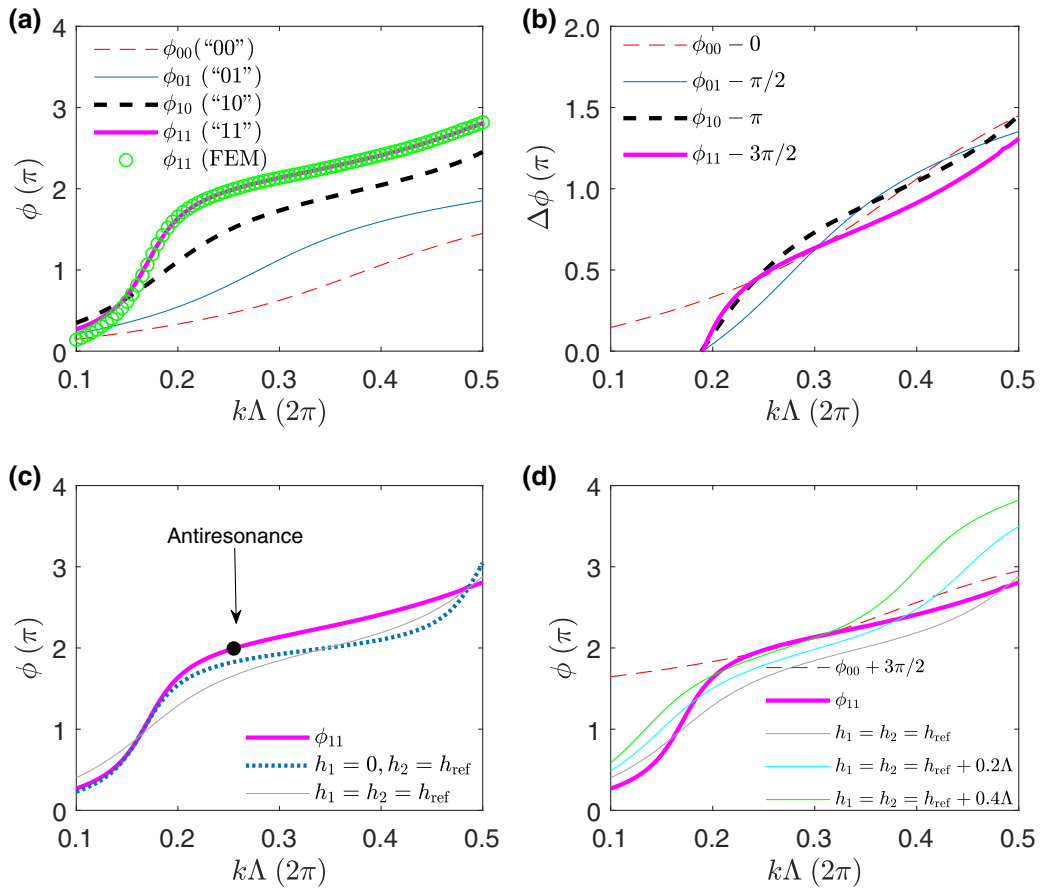
FIG. 2.   (a),(b) Theoretical results of reflection phases of 2-bit coding metasurface elements, where $h_1 = h_2 = 0.6228\Lambda$ for the element "00," $h_1 = h_2 = 0.8697\Lambda$ for "01," $h_1 = h_2 = 1.3\Lambda$ for "10," and $h_1 = 0.4146\Lambda, h_2 = 1.4423\Lambda$ for "11." The simulated reflection phase for the coding element "11" is also marked by empty circles in (a) for comparison, where the thickness of the steel plate is $H = 1.81\Lambda$. (c),(d) Comparisons among the reflection phases of the coding element "11," the unit cell with $h_1 = 0, h_2 = h_{ref}$, and the unit cells with $h_1 = h_2 = h_{ref}$, $h_1 = h_2 = h_{ref} + 0.2\Lambda$, and $h_1 = h_2 = h_{ref} + 0.4\Lambda$, where $h_{ref} = 1.4423\Lambda$ the same as h_2 adopted for the coding element "11." The antiresonance point of the coding element "11" is marked by a filled circle in (c).

phases of 2-bit coding metasurface elements, four subarrays of identical elements are used to form a 2-bit lattice, the dimension of which is $D = 3\Lambda$ [see Fig. 1(b)]. After we get an optimized distribution of elements, the optimized depths of holes of each element [see Fig. 2(a)] are obtained by using a particle swarm optimization algorithm

with a constraint that the average of SCS reduction in the frequency range from $0.2c_0/\Lambda$ to $0.5c_0/\Lambda$ is minimum, where SCS reduction is calculated by the array theory. With the optimized distribution of elements and the optimized depths of holes of each element, Fig. 4 shows SCS reduction calculated by the array theory and
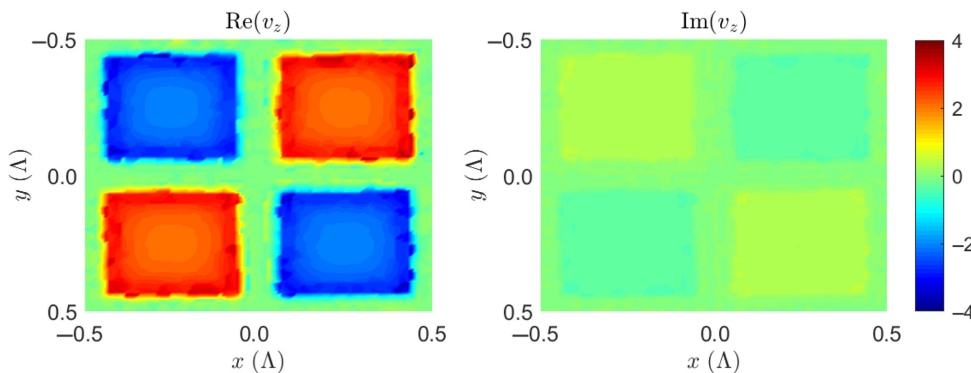

FIG. 3.   Distributions of the real part and imaginary part of normal velocity v_z for a normal incident wave at the frequency of antiresonance marked by a filled circle in Fig. 2(c).
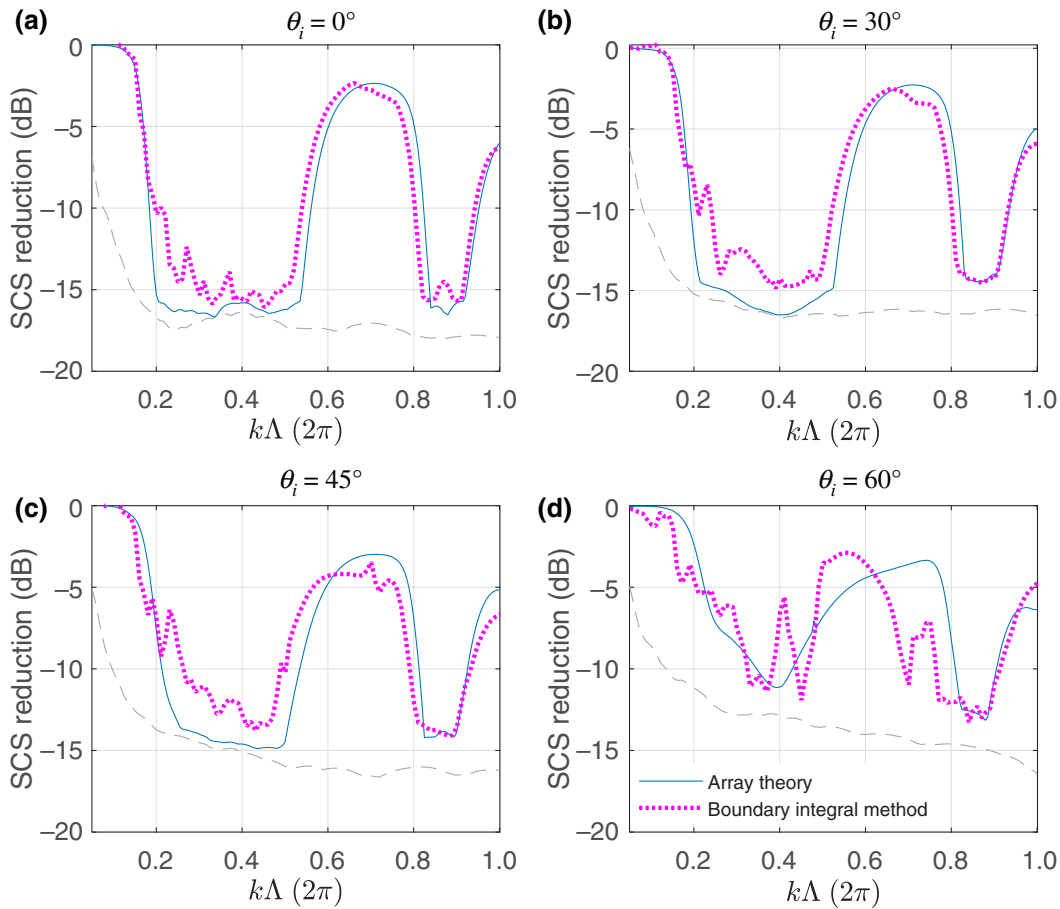
FIG. 4. Dependence of SCS reduction on frequency for the designed 2-bit coding metasurface when plane waves are incident at the elevation and azimuth angles $(\theta_i, 0°)$. For comparisons, results of an ideal 2-bit coding metasurface are also plotted with the dashed gray lines, which are obtained by the array theory.

the boundary integral method. Since the scattering caused by the edge and the back of 2-bit coding metasurface can not be described by the array theory, there exists some differences of predicted SCS reductions by the two methods, and the difference becomes more obvious at large elevation angle θ_i. Note that SCS reduction has a weak dependence on the azimuth angle of incident waves, which has been confirmed by numerical simulations and is not presented here. In addition, because the reflection phase of each element has a dependence on the frequency and incident angle, SCS reduction of the designed metasurface deviates from an ideal 2-bit coding metasurface (see the dashed lines in Fig. 4), however, the performance of SCS reduction is still promising in the designed frequency range from $0.2c_0/\Lambda$ to $0.5c_0/\Lambda$. Note that the ideal 2-bit coding metasurface here means that the reflection phases of coding metasurface elements are $\phi_{00} = 0$, $\phi_{01} = \pi/2$, $\phi_{10} = \pi$ and $\phi_{11} = 3\pi/2$ in the whole frequency range for an arbitrary incident angle, resulting in a good performance of SCS reduction.

To better understand diffusionlike scattering, we define a normalized directivity function as $\overline{\mathrm{Dir}}(\theta, \varphi; \theta_i, \varphi_i) = \lambda^2 \left(4\pi N_x N_y \Lambda^2\right)^{-1} \mathrm{Dir}(\theta, \varphi; \theta_i, \varphi_i)$, where $4\pi N_x N_y \Lambda^2/\lambda^2$ is the theoretical result of maximum directivity of the same sized rigid plate (see Appendix D). Figure 5 illustrates the normalized directivity function of bare plate and 2-bit coding metasurface, which is calculated by the boundary integral method at frequency $0.401c_0/\Lambda$. Owing to the destructive interference among four types of elements, the specular reflection from the bare plate is greatly depressed, and sound waves are scattered diffusely into various directions, resulting in the bistatic SCS suppressed by the coding metasurface.

Then an underwater experiment is carried out to confirm the theoretical prediction. Figure 6(a) shows a 2-bit coding metasurface sample of dimensions 660 mm × 620 mm × 38 mm, which is fabricated by drilling square holes of width $a = 7.5$ mm into a steel plate of thickness $H = 38$ mm $\approx 0.7\lambda_c$, where λ_c denotes the central wavelength of working bandwidth. The designed 2-bit coding

(a) Plate, $\theta_i = 0°$
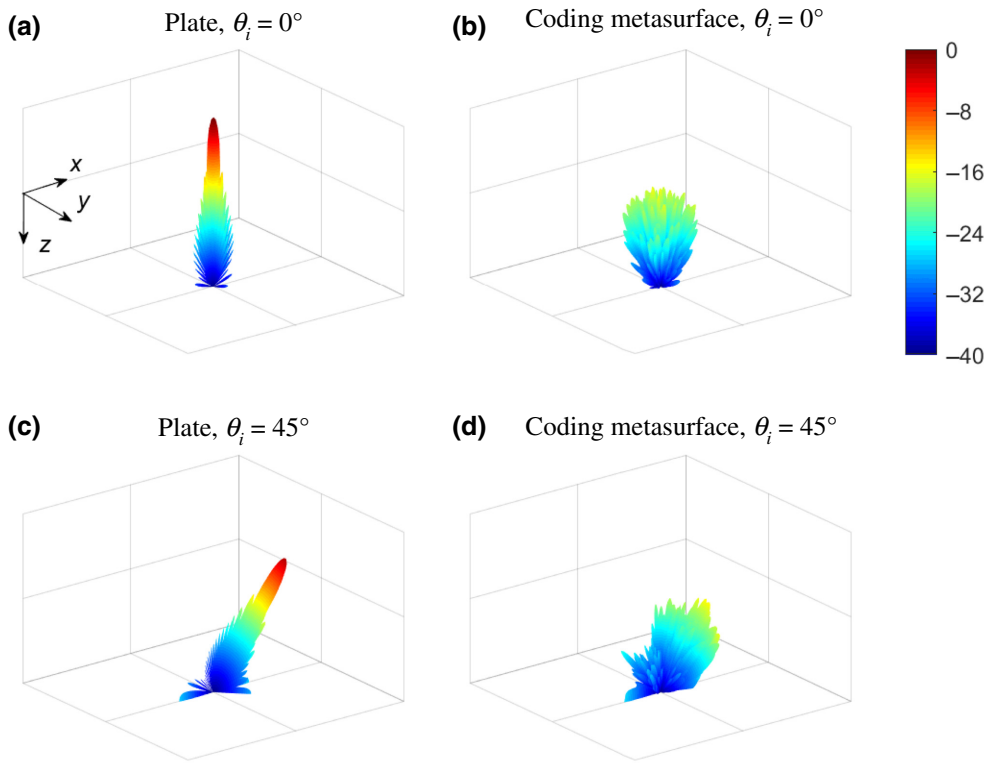
(b) Coding metasurface, $\theta_i = 0°$

FIG. 5. Normalized directivity $10\log_{10}[\overline{\mathrm{Dir}}(\theta, \varphi; \theta_i, \varphi_i)]$ (dB) of bare plate and 2-bit coding metasurface for plane waves incident at the elevation and azimuth angles $(\theta_i, 0°)$.

(c) Plate, $\theta_i = 45°$

(d) Coding metasurface, $\theta_i = 45°$

metasurface consists of an array of 30×30 elements with the size $\Lambda = 20$ mm, where the depths of holes $h_1 = h_2 = 12.46$ mm for the element "00," $h_1 = h_2 = 17.39$ mm for the element "01," $h_1 = h_2 = 26$ mm for the element "10," and $h_1 = 8.29$ mm, $h_2 = 28.85$ mm for the element "11." Figure 6(b) shows a schematic diagram of experimental measurement in an anechoic water tank of dimensions 20 m $\times 12$ m $\times 8$ m. The sound speed determined by the measured temperature is about 1466.6 m/s. The 2-bit coding metasurface, hydrophone, and directional sound source are placed at a depth of 4 m below the water surface. Owing to the large sample size (approximately $12\lambda_c$), the hydrophone and sound source should be placed at a distance r far away from the sample to satisfy the far-field condition, i.e., $r > L^2/\lambda_c$, where L denotes the sample size. Note that only the monostatic measurement is carried out due to the size limitation of tank. The transmitted signals are 20-cycle tone bursts with different central frequencies from 10 to 53 kHz. With the aid of the National Instruments PXI-4480 and PXI-8840, all received signals are obtained with a sampling frequency 1000 kHz, which are averaged by five measurements to improve the signal-to-noise ratio. In order to enhance the signal-to-noise ratio of backscattered waves, the scattered signals are obtained by the subtraction of sound pressure being measured with and without the sample. Figure 6(c) illustrates the measured monostatic SCS of the plate and 2-bit coding metasurface [see Appendix C for the definition in Eq. (C5)], which is consistent with the theoretical prediction by the boundary integral method. It is shown in Fig. 6(d) the measured and

theoretical predicted monostatic SCS reduction, which is the difference between the monostatic SCS of the coding metasurface and the plate. Note that there exists sharp dips in the theoretical predicted monostatic SCS reduction at certain frequencies. This is because that strong destructive interference occurs when the reflection phases satisfy a condition $\phi_{10} - \phi_{00} = \pi, \phi_{11} - \phi_{01} = \pi$. It is shown in Fig. 2(b) that this condition can be approximately satisfied, for example, $\phi_{10} - \phi_{00} = \pi$ at $k\Lambda \approx 0.5 \times 2\pi$ and $\phi_{11} - \phi_{01} = \pi$ at $k\Lambda \approx 0.515 \times 2\pi$, resulting in a sharp dip at $f = 37.47$ kHz ($k\Lambda = 0.511 \times 2\pi$) in Fig. 6(d). Owing to the precision of the fabricated metasurface sample and the experimental error, these dips are not obvious in measurement. For comparison, SCS reduction in Eq. (4) calculated by the boundary integral method is also included, where the directivity is obtained for a sound source located at the position of experiment. It is seen that the bandwidth of SCS reduction below -10 dB covers from $f_L = 14.3$ to $f_H = 40.5$ kHz (from $0.195c_0/\Lambda$ to $0.552c_0/\Lambda$), and the corresponding FBW is defined as FBW $= 2(f_H - f_L)/(f_H + f_L) \approx 95.62\%$, which is verified by the experiment. It is found that the acoustic stealth by our proposed metasurface is encouraging, when it is compared with underwater acoustic carpet cloaks in Refs. [12,13], where 37.04% FBW is obtained for the total SCS reduction around -7 dB by the 2D underwater acoustic carpet cloak [12], and 60% FBW is achieved by the 3D underwater acoustic carpet cloak [13] with the total SCS reduction below -4.8 dB. Note that from the comparison between our result and the radar cross-section reduction
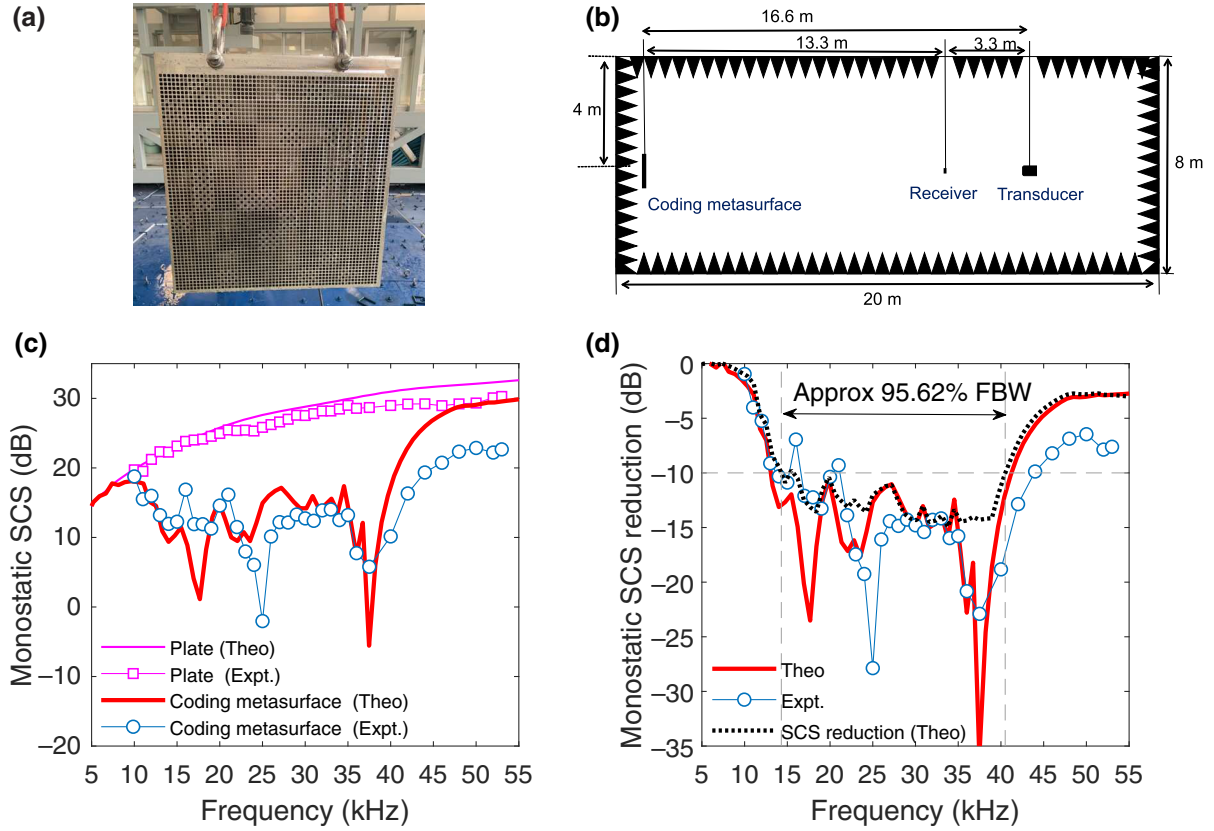
FIG. 6. (a) Photograph of the fabricated 2-bit coding metasurface sample. (b) Schematic diagram of underwater experimental measurement. (c) Monostatic SCS of the bare plate and 2-bit coding metasurface, where solid lines are for theoretical results and markers are for experimental measurements. (d) Theoretical and experimental results for the monostatic SCS reduction, where the calculated SCS reduction is also presented for comparison.

(RCS), in which the FBW of RCS below -10 dB lies in the range from 41% to 148.4% (see Table I in Ref [48]), we infer that FBW might be further improved in future using a more complex design.

IV. CONCLUSION

In conclusion, an underwater broadband 2-bit coding metasuface is developed to reduce the SCS. Both theoretical and experimental results show that SCS reduction can be below -10 dB over a broad frequency band with an approximate 95.62% FBW. Different from carpet cloaks or metasurface carpet cloaks, the mechanism of destructive interference plays a role in acoustic stealth and no reflective surface is needed. Since the performance of the proposed acoustic stealth depends only on the relative reflection phases of coding elements, the concealed object can be located at any position away from the reflective surface. On the other hand, the SCS reduction is valid in a wide range of incident angles. Therefore, our designed 2-bit coding metasurface can be applied to the underwater moving targets. In principle, the nonplanar 2-bit coding metasurface can also be designed based on the destructive interferences, see an example in Appendix

E. It is found that the elevation angle of incident waves in local coordinates can be increased or decreased by the incline angle β of the surface, resulting in the reduction of the elevation angle range in which the required local reflection phase can be satisfied. Therefore, the performance of cloaking is guaranteed with the incline angle β being not very large. On the other hand, the inclined surface with a larger area is preferred to obtain a better SCS reduction performance due to the destructive interferences.

APPENDIX A: DERIVATION OF REFLECTION COEFFICIENT

We assume a unit incident sound pressure,

$$p_{\text{inc}} = \exp(jk\sin\theta_i\cos\varphi_i x + jk\sin\theta_i\sin\varphi_i y + jk\cos\theta_i z), \tag{A1}$$

where (θ_i, φ_i) represent the elevation and azimuth angles of incident waves. According to Floquet's theory, sound fields on the side $(z < 0)$ can be expanded in series,

$$p = p_{\text{inc}} + \sum_{n,m} r_{nm} \exp(jk\beta_n x + jk\alpha_m y - jk_{znm}z), \quad \text{(A2)}$$

where r_{nm} is the reflection coefficient of the (n, m)th diffraction order for $n = 0, \pm1, \pm2, \ldots$, and $m = 0, \pm1, \pm2, \ldots$, $k\beta_n = k \sin\theta_i \cos\varphi_i + 2\pi n / \Lambda$ the horizontal component of wave number along the x axis, $k\alpha_m = k \sin\theta_i \sin\varphi_i + 2\pi m / \Lambda$ the horizontal component of wave number along the y axis, and $k_{znm} = \sqrt{k^2 - (k\beta_n)^2 - (k\alpha_m)^2}$ the vertical component of wave number.

Using the equation of motion $jk\rho cu = \partial p / \partial z$ and Eq. (A2), the vertical velocity component u at the boundary $z = 0$ can be described as

$$jk\rho cu(x, y, 0) = jk_{z00} \exp(jk\beta_0 x + jk\alpha_0 y)$$
$$- \sum_{n,m} r_{nm} jk_{znm} \exp(jk\beta_n x + jk\alpha_m y). \quad \text{(A3)}$$

By the continuity of normal velocity and the orthogonality of function $\exp(jk\beta_n x + jk\alpha_m y)$, we obtain from Eq. (A3),

$$\Lambda^2 (k_{z00}\delta_{0n}\delta_{0m} - k_{znm}r_{nm}) / (k\rho c)$$
$$= U_1\Phi_{1nm} + U_2\Phi_{2nm} + U_3\Phi_{3nm} + U_4\Phi_{4nm}, \quad \text{(A4)}$$

where δ_{0n} is the Kronecker δ, $U_i (i = 1, 2, 3, 4)$ are the volume velocities of four square holes marked in Fig. 1(a), which are defined as $U_i = \iint_{S_i} u(x, y, 0)dxdy$, and $\Phi_{inm} = (1/S_i) \iint_{S_i} \exp(-jk\beta_n x - jk\alpha_m y)dxdy$. Note that the plane-wave approximation is adopted for the waves in holes for the working frequency lower than the cutoff. The reflection coefficient is then derived from Eq. (A4),

$$r_{nm} = \delta_{0n}\delta_{0m} - R_{nm}[U_1\Phi_{1nm}$$
$$+ U_2\Phi_{2nm} + U_3\Phi_{3nm} + U_4\Phi_{4nm}], \quad \text{(A5)}$$

with $R_{nm} = \rho c / (\Lambda^2 \sqrt{1 - \beta_n^2 - \alpha_m^2})$. By substituting Eq. (A5) into Eq. (A2), and using the continuity of sound pressure at the boundary $z = 0$, we have,

$$\begin{aligned}
2\Phi_{100}^* - \bar{p}_1 &= Z_{11}U_1 + Z_{12}U_2 + Z_{13}U_3 + Z_{14}U_4,\\
2\Phi_{200}^* - \bar{p}_2 &= Z_{21}U_1 + Z_{22}U_2 + Z_{23}U_3 + Z_{24}U_4,\\
2\Phi_{300}^* - \bar{p}_3 &= Z_{31}U_1 + Z_{32}U_2 + Z_{33}U_3 + Z_{34}U_4,\\
2\Phi_{400}^* - \bar{p}_4 &= Z_{41}U_1 + Z_{42}U_2 + Z_{43}U_3 + Z_{44}U_4,
\end{aligned} \quad \text{(A6)}$$

where the asterisk $*$ means complex conjugate, $\bar{p}_i = (1/S_i) \iint_{S_i} p(x, y, 0)dxdy$ an average pressure for each

hole, and $Z_{iq} = \sum_{n,m} R_{nm}\Phi_{inm}^*\Phi_{qnm}$ for $i = 1, 2, 3, 4$ and $q = 1, 2, 3, 4$. Note that the average pressure at the inlet of each hole can be related to the volume velocity, $\bar{p}_i = Z_{a_i}U_i$, in which acoustic impedance is $Z_{ai} = j\rho c / [a^2 \tan(kl_i)]$ with l_i being the depth of each hole and a the side length.

By substituting U_i [the solution of Eq. (A6)] into Eq. (A5), we get the reflection coefficient r_{00}, from which the local phase ϕ of reflected waves can be extracted. Note that the reflection coefficient r_{00} obtained at the large elevation angle θ_i is not very accurate, especially when the averages of normal velocity and pressure over the inlet of hole become invalid at high frequency.

APPENDIX B: DERIVATION OF THE FAR-FIELD SCATTERING AMPLITUDE FROM THE BOUNDARY INTEGRAL METHOD

Using Green's theorem, the total pressure in the exterior region is

$$p(\vec{r}) = p_{\text{inc}}(\vec{r}) + \iint_{S'} G(\vec{r}, \vec{r}') \frac{\partial p(\vec{r}')}{\partial n'}$$
$$- \frac{\partial G(\vec{r}, \vec{r}')}{\partial n'} p(\vec{r}') dS', \quad \text{(B1)}$$

where p_{inc} represents an incident plane wave or the sound field generated by a source, $G(\vec{r}, \vec{r}') = (1/4\pi |\vec{r} - \vec{r}'|)e^{jk|\vec{r}-\vec{r}'|}$ denotes Green's function for the Helmholtz equation in free space, and $\vec{n}'$ points to the interior region of coding metasurface, the thickness of which is H. For simplification, the metasurface is in the shape of a cuboid, and its exterior surface S' is divided into two parts, $S' = S_1' \cup S_2'$, where S_1' corresponds to the face with the drilled holes, i.e., the plane at $z = 0$ in Fig. 1(b), and S_2' means the other five faces of the cuboid. Owing to the assumption of the rigid surface, $[\partial p(\vec{r}')/\partial n'] = 0$ is satisfied for $\vec{r}' \in S_2'$, while for $\vec{r}' \in S_1'$, $[\partial p(\vec{r}')/\partial n'] = [\partial p(\vec{r}')/\partial z']|_{z'=0} = jk\rho_0 c_0 u_z|_{z'=0}$ is obtained by the equation of motion, and $u_z|_{z'=0} \neq 0$ for the positions located in holes, otherwise, $u_z|_{z'=0} = 0$. Therefore, Eq. (B1) can be rewritten as

$$p(\vec{r}) = p_{\text{inc}}(\vec{r}) + \iint_{(x',y',0)\in S_{\text{hole}}} G(\vec{r}, \vec{r}') \frac{jk\rho_0 c_0}{Z_s(x', y')} p(\vec{r}')|_{z'=0}dS'$$
$$- \iint_{(x',y',z')\in S'} \frac{\partial G(\vec{r}, \vec{r}')}{\partial n'} p(\vec{r}') dS', \quad \text{(B2)}$$

where S_{hole} denotes the region occupied by holes, $Z_s(x', y')$ represents the specific acoustic impedance at the inlet of hole. It is seen from Eq. (B2) that the pressure $p(\vec{r})$ at an arbitrary position in the exterior region of coding metasurface can be determined by the pressure $p(\vec{r}')$ on the

exterior surface S'. Let $\vec{r}$ in Eq. (B2) approach the exterior surface S', the values of $p(\vec{r}')$ can be obtained by

$$
\begin{aligned}
C(\vec{r}) p(\vec{r}) &= p_{\text{inc}}(\vec{r}) \\
&+ \iint\limits_{(x',y',0)\in S_{\text{hole}}} G(\vec{r},\vec{r}') \frac{jk\rho_0 c_0}{Z_s(x',y')} p(\vec{r}')|_{z'=0} dS' \\
&- \iint\limits_{(x',y',z')\in S'} \frac{\partial G(\vec{r},\vec{r}')}{\partial n'} p(\vec{r}') dS',
\end{aligned}
\tag{B3}
$$

where $C(\vec{r}) = 1/2$ when $\vec{r}$ is located at the surface S', and $C(\vec{r}) = 0$ when $\vec{r}$ is located in the interior region surrounded by the surface S'. By discretizing the integral Eq. (B3), we obtain the overdetermined linear equations, which are solved by the method of least squares.

In order to obtain the far-field scattering amplitude, Green's function and its normal derivative in the far field can be approximated as

$$
\begin{aligned}
G(\vec{r},\vec{r}') &\approx \frac{\exp(jkr - j\vec{k}\cdot\vec{r}')}{4\pi r}, \frac{\partial G(\vec{r},\vec{r}')}{\partial n'} \\
&\approx -j\vec{n}'\cdot\vec{k}\frac{\exp(jkr - j\vec{k}\cdot\vec{r}')}{4\pi r},
\end{aligned}
\tag{B4}
$$

where $\vec{k} = k(\sin\theta\cos\varphi, \sin\theta\sin\varphi, \cos\theta)$ denotes the wave vector, and (θ, φ) represent the elevation and azimuth angles of the position vector $\vec{r}$. Substituting Eq. (B4) into Eq. (B2), the scattered pressure field can approximated as

$$
p_{\text{sca}}(\vec{r}) = p(\vec{r}) - p_{\text{inc}}(\vec{r}) \approx f(\theta,\varphi;\theta_i,\varphi_i) \frac{\exp(jkr)}{r}.
\tag{B5}
$$

For an incident plane wave $p_{\text{inc}} = \exp(jk\sin\theta_i\cos\varphi_i x + jk\sin\theta_i\sin\varphi_i y + jk\cos\theta_i z)$, $f(\theta,\varphi;\theta_i,\varphi_i)$ represents the far-field scattering amplitude,

$$
f(\theta,\varphi;\theta_i,\varphi_i) \approx \frac{1}{4\pi}\left[\iint\limits_{(x',y',0)\in S_{\text{hole}}} \exp(-j\vec{k}\cdot\vec{r}')\frac{jk\rho_0 c_0}{Z_s(x',y')} p(\vec{r}')|_{z'=0} dS' + \iint\limits_{(x',y',z')\in S'} j\vec{n}'\cdot\vec{k}\exp(-j\vec{k}\cdot\vec{r}')p(\vec{r}') dS' \right]
\tag{B6}
$$

APPENDIX C: THE RELATION BETWEEN SCS REDUCTION AND THE FAR-FIELD SCATTERING AMPLITUDE

The scattering cross section is usually adopted to describe the scattering of a plane wave by an object, which is defined as

$$
\sigma(\theta,\varphi;\theta_i,\varphi_i) = \lim_{r\to\infty} 4\pi r^2 \left|\frac{p_{\text{sca}}}{p_{\text{inc}}}\right|^2.
\tag{C1}
$$

Substituting Eq. (B5) into Eq. (C1), the scattering cross section can be rewritten as

$$
\sigma(\theta,\varphi;\theta_i,\varphi_i) = 4\pi|f(\theta,\varphi;\theta_i,\varphi_i)|^2.
\tag{C2}
$$

Relative to a rigid plate with the same size, the SCS reduction caused by the coding metasurface is obtained as

$$
\begin{aligned}
\sigma_R &= 10\log_{10}\left(\underset{\theta,\varphi}{\text{Max}}\left[|\sigma(\theta,\varphi;\theta_i,\varphi_i)||_{\text{coded}}\right] \Big/ \underset{\theta,\varphi}{\text{Max}}\left[|\sigma(\theta,\varphi;\theta_i,\varphi_i)||_{\text{bare}}\right]\right) \\
&= 10\log_{10}\left(\underset{\theta,\varphi}{\text{Max}}\left[|f(\theta,\varphi;\theta_i,\varphi_i)|^2|_{\text{coded}}\right] \Big/ \underset{\theta,\varphi}{\text{Max}}\left[|f(\theta,\varphi;\theta_i,\varphi_i)|^2|_{\text{bare}}\right]\right).
\end{aligned}
\tag{C3}
$$

As the scattering energy by the coding metasurface is the same as the rigid plate, we have $\int_0^{2\pi}\int_{(\pi/2)}^{\pi}|f(\theta,\varphi;\theta_i,\varphi_i)|^2\sin\theta d\theta d\varphi = \text{constant}$, resulting in

$$
\sigma_R = 10\log_{10}\left(\frac{\underset{\theta,\varphi}{\text{Max}}\left[\text{Dir}(\theta,\varphi;\theta_i,\varphi_i)|_{\text{coded}}\right]}{\underset{\theta,\varphi}{\text{Max}}\left[\text{Dir}(\theta,\varphi;\theta_i,\varphi_i)|_{\text{bare}}\right]}\right).
\tag{C4}
$$

Note that the difference between these two definitions [Eq. (C3) and (C4)] can be neglected, which has been confirmed by numerical results.

Using Eq. (C2), we also define the physical quantities measured in experiment, one is the monostatic SCS,

$$\sigma^{\mathrm{mono}} = 10 \log_{10} \left(4\pi \, |f \, (\theta = \pi, \varphi = 0; \theta_i = 0, \varphi_i = 0)|^2 \right), \tag{C5}$$

and the other is monostatic SCS reduction,

$$\sigma_R^{\mathrm{mono}} = 10 \log_{10} \left(\frac{|f \, (\theta = \pi, \varphi = 0; \theta_i = 0, \varphi_i = 0)|^2 \, |_{\mathrm{coded}}}{|f \, (\theta = \pi, \varphi = 0; \theta_i = 0, \varphi_i = 0)|^2 \, |_{\mathrm{bare}}} \right), \tag{C6}$$

where the far-field backscattering amplitude in experiment is obtained as $|f \, (\theta = \pi, \varphi = 0; \theta_i = 0, \varphi_i = 0)| = |p_{\mathrm{sca}} r_1 r_2 / [p_{\mathrm{inc}} \, (r_1 - r_2)]|$, where p_{inc} means the direct waves received by a hydrophone, p_{sca} denotes the scattered waves received by the same hydrophone, and r_1 and r_2 represents the distances of a source and a hydrophone away from the coding metasurface (or rigid plate), respectively.

APPENDIX D: THE DIRECTIVITY OF RIGID PLATE

For a plane wave normally incident upon a rigid plate of radius R, the far-field scattering amplitude is approximated as

$$f \, (\theta, \varphi; \theta_i, \varphi_i) \propto \frac{2J_1 \, (kR \sin \theta)}{kR \sin \theta}, \tag{D1}$$

where the directional factor of radiation from a circular piston is adopted. For $kR \gg 1$, and using the definition of directivity in Eq. (3), we obtain

$$\mathrm{Dir} \, (\theta, \varphi; 0, 0) \approx \frac{4\pi S}{\lambda^2} \left[\frac{2J_1 \, (kR \sin \theta)}{kR \sin \theta} \right]^2, \tag{D2}$$

with $S = \pi R^2$ the area of rigid plate. It is seen from Eq. (D2) that

$$\underset{\theta, \varphi}{\mathrm{Max}} \, [\mathrm{Dir} \, (\theta, \varphi; 0, 0)] \approx \frac{4\pi S}{\lambda^2}. \tag{D3}$$

APPENDIX E: THE CLOAKING EFFECT OF A NONPLANAR 2-BIT CODING METASURFACE

For a nonplanar surface illustrated in Fig. 7(a), which is described as

$$z = \begin{cases} -13\Lambda, (0 < |x| < 3\Lambda, 0 < |y| < 15\Lambda) \\ -13\Lambda + (|x| - 3\Lambda) \tan \beta, (3\Lambda < |x| < 31\Lambda, 0 \\ \quad < |y| < 15\Lambda), \end{cases} \tag{E1}$$

with an incline angle $\beta = \arctan(13/28) \approx 24.9°$. For the scattering caused by a nonplanar surface S', the array pattern can be expressed as

$$S \, (\theta, \varphi; \theta_i, \varphi_i) \propto \int_{\vec{r}' \in S'}$$
$$\exp \left[j \phi \left(\vec{k}_i, \vec{r}' \right) \right] \exp \left[-j \left(\vec{k} - \vec{k}_i \right) \cdot \vec{r}' \right] dS', \tag{E2}$$

where $\vec{k} = k \, (\sin \theta \cos \varphi, \sin \theta \sin \varphi, \cos \theta)$ represents the wave vector of scattered waves, $\vec{k}_i = k \, (\sin \theta_i \cos \varphi_i, \sin \theta_i \sin \varphi_i, \cos \theta_i)$ the wave vector of incident waves, $\vec{r}' = (x', y', z')$ the position vector of a point on S', and $\phi \left(\vec{k}_i, \vec{r}' \right)$ the local reflection phase, which can be easily obtained in local coordinates, for example, the $x_r o_r z_r$ plane marked in Fig. 7(a). When the nonplanar surface is cloaked with 2-bit coding metasurface elements, the integral in Eq. (E2) can be written in a summation form similar to Eq. (2). With the help of Eq. (E2), the SCS reduction defined in Eq. (4) can be calculated with the directivity $\mathrm{Dir}(\theta, \varphi; \theta_i, \varphi_i)$ being revised for the nonplanar metasurface, i.e., $\mathrm{Dir} \, (\theta, \varphi; \theta_i, \varphi_i) = 4\pi \, |f \, (\theta, \varphi; \theta_i, \varphi_i)|^2 / \int_0^{2\pi} \int_0^{\pi} |f \, (\theta, \varphi; \theta_i, \varphi_i)|^2 \sin \theta d\theta d\varphi$, where $|f \, (\theta, \varphi; \theta_i, \varphi_i)| = 0$ is chosen when the shadowing occurs, which is consistent with the definition for the planar metasurface in Eq. (3).

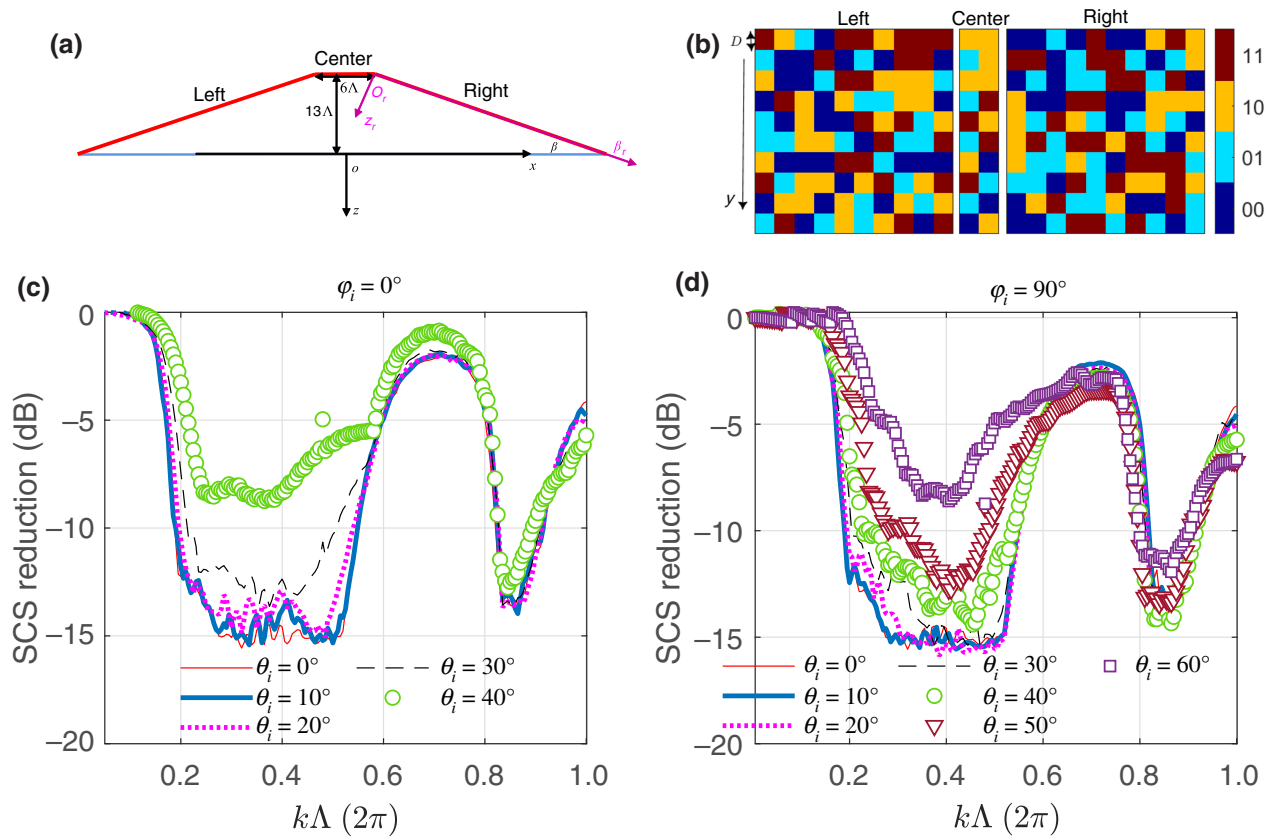Similar to the design procedure adopted above, we obtain a distribution of 2-bit coding metasurface elements

FIG. 7.   (a) Cross-section illustration of a nonplanar surface with an incline angle $\beta \approx 24.9°$. (b) The distribution of 2-bit coding metasurface elements on the nonplanar surface in (a). (c),(d) Dependence of SCS reduction on frequency when plane waves are incident at different elevation angles θ_i but at the same azimuth angle $\varphi_i = 0°$ in (c) and $\varphi_i = 90°$ in (d).

in Fig. 7(b) for the nonplanar surface in Fig. 7(a). Figures 7(c) and 7(d) show the SCS reduction calculated by the array theory, in which the parameters of 2-bit coding metasurface elements are the same as that in Fig. 2. Different from the planar metasurface, the SCS reduction has an obvious dependence on the azimuth angle of incident waves. It is found that the performance of SCS reduction at the azimuth angle $\varphi_i = 90°$ (or $\varphi_i = 270°$) is better than that at $\varphi_i = 0°$ (or $\varphi_i = 180°$). This is because the elevation angle of incident waves in the $x_r o_r z_r$ plane is increased to $\theta_i + \beta$ for $\theta_i > 0, \varphi_i = 0°$, resulting in the reduction of the elevation angle range in which the required local reflection phase can be satisfied. In other words, the performance of SCS reduction is satisfactory at all incident azimuth angles for $\theta_i < 30°$.

[1] U. Leonhardt, Optical conformal mapping, Science **312**, 1777 (2006).

[2] J. B. Pendry, D. Schurig, and D. R. Smith, Controlling electromagnetic fields, Science **312**, 1780 (2006).

[3] G. W. Milton, M. Briane, and J. R. Willis, On cloaking for elasticity and physical equations with a transformation invariant form, New J. Phys. **8**, 248 (2006).

[4] S. A. Cummer and D. Schurig, One path to acoustic cloaking, New J. Phys. **9**, 45 (2007).

[5] H. Chen and C. T. Chan, Acoustic cloaking in three dimensions using acoustic metamaterials, Appl. Phys. Lett. **91**, 183518 (2007).

[6] A. N. Norris, Acoustic cloaking theory, Proc. R. Soc. A. **464**, 2411 (2008).

[7] S. A. Cummer, B.-I. Popa, D. Schurig, D. R. Smith, J. Pendry, M. Rahm, and A. Starr, Scattering Theory Derivation of a 3D Acoustic Cloaking Shell, Phys. Rev. Lett. **100**, 024301 (2008).

[8] D. Torrent and J. Sánchez-Dehesa, Acoustic cloaking in two dimensions: A feasible approach, New. J. Phys. **10**, 063015 (2008).

[9] S. Zhang, C. Xia, and N. Fang, Broadband Acoustic Cloak for Ultrasound Waves, Phys. Rev. Lett. **106**, 024301 (2011).

[10] B. I. Popa, L. Zigoneanu, and S. A. Cummer, Experimental Acoustic Ground Cloak in air, Phys. Rev. Lett. **106**, 253901 (2011).

[11] L. Zigoneanu, B. I. Popa, and S. A. Cummer, Three-dimensional broadband omnidirectional acoustic ground cloak, Nat. Mater. **13**, 352 (2014).

[12] Y. Bi, H. Jia, W. Lu, P. Ji, and J. Yang, Design and demonstration of an underwater acoustic carpet cloak, Sci. Rep. **7**, 705 (2017).

[13] Y. Bi, H. Jia, Z. Sun, Y. Yang, H. Zhao, and J. Yang, Experimental demonstration of three-dimensional broadband

underwater acoustic carpet cloak, Appl. Phys. Lett. **112,** 223502 (2018).

[14] C. Faure, O. Richoux, S. Félix, and V. Pagneux, Experiments on metasurface carpet cloaking for audible acoustics, Appl. Phys. Lett. **108,** 064103 (2016).

[15] Y. Yang, H. Wang, F. Yu, Z. Xu, and H. Chen, A metasurface carpet cloak for electromagnetic, acoustic and water waves, Sci. Rep. **6,** 20219 (2016).

[16] X. Wang, D. Mao, and Y. Li, Broadband acoustic skin cloak based on spiral metasurfaces, Sci. Rep. **7,** 11604 (2017).

[17] M. Amin, O. Siddiqui, W. Orfali, M. Farhat, and A. Khelif, Resonant Beam Steering and Carpet Cloaking Using an Acoustic Transformational Metascreen, Phys. Rev. Appl. **10,** 064030 (2018).

[18] W. Ji, Q. Wei, X. Zhu, and D. Wu, 3D acoustic metasurface carpet cloak based on groove structure units, J. Phys. D: Appl. Phys. **52,** 325302 (2019).

[19] Y. Jin, X. Fang, Y. Li, and D. Torrent, Engineered Diffraction Gratings for Acoustic Cloaking, Phys. Rev. Appl. **11,** 011004 (2019).

[20] J. He, X. Jiang, D. Ta, and W. Wang, Experimental demonstration of underwater ultrasound cloaking based on metagrating, Appl. Phys. Lett. **117,** 091901 (2020).

[21] A. Alù and N. Engheta, Achieving transparency with plasmonic and metamaterial coatings, Phys. Rev. E **72,** 016623 (2005).

[22] M. D. Guild, A. Alù, and M. R. Haberman, Cancellation of acoustic scattering from an elastic sphere, J. Acoust. Soc. Am. **129,** 1355 (2011).

[23] L. Sanchis, V. M. García-Chocano, R. Llopis-Pontiveros, A. Climente, J. Martínez-Pastor, F. Cervera, and J. Sánchez-Dehesa, Three-Dimensional Axisymmetric Cloak Based on the Cancellation of Acoustic Scattering from a Sphere, Phys. Rev. Lett. **110,** 124301 (2013).

[24] M. D. Guild, A. Alù, and M. R. Haberman, Cloaking of an acoustic sensor using scattering cancellation, Appl. Phys. Lett. **105,** 023510 (2014).

[25] C. A. Rohde, T. P. Martin, M. D. Guild, C. N. Layman, C. J. Naify, M. Nicholas, A. L. Thangawng, D. C. Calvo, and G. J. Orris, Experimental demonstration of underwater acoustic scattering cancellation, Sci. Rep. **5,** 13175 (2015).

[26] Z. Gu, B. Liang, X. Zou, and J. C. Cheng, Broadband diffuse reflections of sound by metasurface with random phase response, EPL **111,** 64003 (2015).

[27] Y. F. Zhu, X. D. Fan, B. Liang, J. C. Cheng, and Y. Jing, Ultrathin Acoustic Metasurface-Based Schroeder Diffuser, Phys. Rev. X **7,** 021034 (2017).

[28] N. Jiménez, T. J. Cox, V. Romero-García, and J. P. Groby, Metadiffusers: Deep-subwavelength sound diffusers, Sci. Rep. **7,** 5389 (2017).

[29] W. Cao, L. Wu, C. Zhang, J. C. Ke, Q. Cheng, and T. J. Cui, A reflective acoustic meta-diffuser based on the coding meta-surface, J. Appl. Phys. **126,** 194503 (2019).

[30] E. Ballestero, N. N. Jiménez, J.-P. Groby, S. Dance, H. Aygun, and V. Romero-García, Experimental validation of deep-subwavelength diffusion by acoustic metadiffusers, Appl. Phys. Lett. **115,** 081901 (2019).

[31] C. D. Giovampaola and N. Engheta, Digital metamaterials, Nat. Mater. **13,** 1115 (2014).

[32] T. J. Cui, M. Q. Qi, X. Wan, J. Zhao, and Q. Cheng, Coding metamaterials, digital metamaterials and programmable metamaterials, Light Sci. Appl. **3,** e218 (2014).

[33] L. Liang, M. Qi, J. Yang, X. Shen, J. Zhai, W. Xu, B. Jin, W. Liu, Y. Feng, C. Zhang, H. Lu, H.-T. Chen, L. Kang, W. Xu, J. Chen, T. J. Cui, P. Wu, and S. Liu, Anomalous terahertz reflection and scattering by flexible and conformal coding metamaterials, Adv. Opt. Mater. **3,** 1374 (2015).

[34] L.-H. Gao, Q. Cheng, J. Yang, S.-J. Ma, J. Zhao, S. Liu, H.-B. Chen, Q. He, W.-X. Jiang, H.-F. Ma, Q.-Y. Wen, L.-J. Liang, B.-B. Jin, W.-W. Liu, L. Zhou, J.-Q. Yao, P.-H. Wu, and T.-J. Cui, Broadband diffusion of terahertz waves by multi-bit coding metasurfaces, Light Sci. Appl. **4,** e324 (2015).

[35] M. Moccia, S. Liu, R. Y. Wu, G. Castaldi, A. Andreone, T. J. Cui, and V. Galdi, Coding metasurfaces for diffuse scattering: Scaling laws, bounds, and suboptimal design, Adv. Opt. Mater. **5,** 1700455 (2017).

[36] K. Chen, L. Cui, Y. Feng, J. Zhao, T. Jiang, and B. Zhu, Coding metasurface for broadband microwave scattering reduction with optical transparency, Opt. Express. **25,** 5571 (2017).

[37] M. Moccia, C. Koral, G. P. Papari, S. Liu, L. Zhang, R. Y. Wu, G. Castaldi, T. J. Cui, V. Galdi, and A. Andreone, Suboptimal coding metasurfaces for terahertz diffuse scattering, Sci. Rep. **8,** 11908 (2018).

[38] B. Sima, K. Chen, X. Luo, J. Zhao, and Y. Feng, Combining Frequency-Selective Scattering and Specular Reflection through Phase-Dispersion Tailoring of a Metasurface, Phys. Rev. Appl. **10,** 064043 (2018).

[39] B. Xie, K. Tang, H. Cheng, Z. Liu, S. Chen, and J. Tian, Coding acoustic metasurfaces, Adv. Mater. **29,** 1603507 (2017).

[40] B. Xie, H. Cheng, K. Tang, Z. Liu, S. Chen, and J. Tian, Multiband Asymmetric Transmission of Airborne Sound by Coded Metasurfaces, Phys. Rev. Appl. **7,** 024010 (2017).

[41] D. Chen, X. Zhu, D. Wu, and X. Liu, Broadband airy-like beams by coded acoustic metasurfaces, Appl. Phys. Lett. **114,** 053504 (2019).

[42] S. Zuo, Y. Cheng, and X. Liu, Tunable perfect negative reflection based on an acoustic coding metasurface, Appl. Phys. Lett. **114,** 203505 (2019).

[43] Y. Zhang, B. Xie, W. Liu, H. Cheng, S. Chen, and J. Tian, Anomalous reflection and vortex beam generation by multi-bit coding acoustic metasurfaces, Appl. Phys. Lett. **114,** 091905 (2019).

[44] H. Gao, Z. Gu, S. Liang, S. An, T. Liu, and J. Zhu, Coding Metasurface for Talbot Sound Amplification, Phys. Rev. Appl. **14,** 054067 (2020).

[45] P. Wang, G. Yu, Y. Li, X. Wang, and N. Wang, Achromatic reflected metalens for highly directional and long distance acoustic probing, New J. Phys. **22,** 023006 (2020).

[46] Y. Dong, G. Yu, and N. Wang, Robust far-field subwavelength imaging of scatterers by an acoustic superlens, J. Acoust. Soc. Am. **146,** 4131 (2019).

[47] R. Poli, J. Kennedy, and T. Blackwell, Particle swarm optimization, Swarm Intell. **1,** 33 (2007).

[48] J. Su, H. He, Y. Lu, H. Yin, G. Liu, and Z. Li, Ultrawideband Radar Cross-Section Reduction by a Metasurface Based on Defect Lattices and Multiwave Destructive Interference, Phys. Rev. Appl. **11,** 044088 (2019).